The Astrophysical Journal, 704:485–495, 2009 October 10 doi:10.1088/0004-637X/704/1/485

FAN–SPINE TOPOLOGY FORMATION THROUGH TWO-STEP RECONNECTION DRIVEN BY TWISTED FLUX EMERGENCE

T. Török[1], G. Aulanier[1], B. Schmieder[1], K. K. Reeves[2], and L. Golub[2]
[1] LESIA, Observatoire de Paris, CNRS, UPMC, Université Paris Diderot, 5 place Jules Janssen, 92190 Meudon, France
[2] Harvard-Smithsonian Center for Astrophysics, 60 Garden Street, Cambridge, MA 02138, USA
Received 2009 May 13; accepted 2009 August 26; published 2009 September 23

ABSTRACT

We address the formation of three-dimensional nullpoint topologies in the solar corona by combining *Hinode*/X-ray Telescope (XRT) observations of a small dynamic limb event, which occurred beside a non-erupting prominence cavity, with a three-dimensional (3D) zero-β magnetohydrodynamics (MHD) simulation. To this end, we model the boundary-driven "kinematic" emergence of a compact, intense, and uniformly twisted flux tube into a potential field arcade that overlies a weakly twisted coronal flux rope. The expansion of the emerging flux in the corona gives rise to the formation of a nullpoint at the interface of the emerging and the pre-existing fields. We unveil a two-step reconnection process at the nullpoint that eventually yields the formation of a broad 3D fan–spine configuration above the emerging bipole. The first reconnection involves emerging fields and a set of large-scale arcade field lines. It results in the launch of a torsional MHD wave that propagates along the arcades, and in the formation of a sheared loop system on one side of the emerging flux. The second reconnection occurs between these newly formed loops and remote arcade fields, and yields the formation of a second loop system on the opposite side of the emerging flux. The two loop systems collectively display an anenome pattern that is located below the fan surface. The flux that surrounds the inner spine field line of the nullpoint retains a fraction of the emerged twist, while the remaining twist is evacuated along the reconnected arcades. The nature and timing of the features which occur in the simulation do qualititatively reproduce those observed by XRT in the particular event studied in this paper. Moreover, the two-step reconnection process suggests a new consistent and generic model for the formation of anemone regions in the solar corona.

Key words: methods: numerical – MHD – Sun: corona – Sun: magnetic fields

Online-only material: animations

1. INTRODUCTION

Various dynamic phenomena in the solar corona, such as soft X-ray jets and specific flares, have been associated with magnetic reconnection occurring in a three-dimensional (3D) magnetic nullpoint topology consisting of a dome-like fan separatrix surface located below the nullpoint and a spine field line above it (e.g., Lau & Finn 1990; Antiochos 1998; Priest & Forbes 2002). Observational evidence of 3D nullpoint topologies in the corona is provided by, e.g., "saddle-like" loop structures (Filippov 1999), "ellipsoidal flare ribbons" (Masson et al. 2009), and "anemone" active regions within coronal holes (Shibata et al. 1992a). The latter are characterized by a full or partial ring of radially aligned bright loops which connect the opposite polarities of the region and the surrounding coronal hole (e.g., Asai et al. 2008). Anemone active regions are often associated with soft X-ray jets (e.g., Shibata et al. 1994), which are a strong indication of 3D nullpoint reconnection occurring in the corona. Further evidence for coronal nullpoint topologies comes from subphotospheric source models of the coronal magnetic field (Démoulin et al. 1993), and from potential and linear force-free field extrapolations of flare and jet regions (e.g., Aulanier et al. 2000; Fletcher et al. 2001; Ugarte-Urra et al. 2007; Moreno-Insertis et al. 2008). Consequently, 3D fan–spine configurations are increasingly used as the initial condition in numerical simulations of 3D reconnection, jets, and flares (Pontin et al. 2007; Pariat et al. 2009; Masson et al. 2009). The reconnection is triggered by boundary motions in these simulations.

The *formation* of 3D fan–spine configurations in the corona, however, has not yet been studied in much detail. In potential or near-potential magnetic fields, a 3D nullpoint configuration with a fan and a spine naturally occurs if a magnetic bipole is embedded into one polarity region of a large-scale bipolar ambient field (e.g., Antiochos 1998). Therefore, it is expected to form when magnetic flux emerges into regions of essentially unipolar fields, such as a coronal hole. The fan–spine configuration then results from the relaxation of the coronal field after its reconnection with the emerging flux. Two-dimensional numerical simulations of coronal soft X-ray jets, inspired by the flux emergence model by Heyvaerts et al. (1977), have demonstrated that reconnection between emerging bipolar flux and a vertical or oblique coronal field yields the formation of hot loops connecting the ambient field with the opposite polarity flux of the emerging bipole (e.g., Yokoyama & Shibata 1996; Nishizuka et al. 2008).

Moreno-Insertis et al. (2008) recently performed a 3D simulation of the emergence of a twisted flux tube into an oblique unipolar coronal field. As in the two-dimensional cases, they found the launch of a jet and the formation of a growing system of hot reconnected loops connecting the ambient field with the emerging flux of opposite polarity. The resulting fan surface extends on one side of the emerging region, while on the other side it consists of non-reconnected emerged loops only. The latter are not strongly heated and would hence unlikely be seen in soft X-ray observations, therefore only one-half of an anemone loop pattern should be visible.

Pariat et al. (2009) used an alternative approach to produce a jet, by starting from a 3D nullpoint topology and driving the jet by reconnection between open and closed field lines, after the latter have been significantly twisted by line-tied boundary motions. One outcome of this calculation is that, as a result of reconnection of twisted fields, the nullpoint moved around the axis of the spine, thus allowing reconnection of field lines from all sides of the fan. While this evolution may allow for the brightening of the whole fan in soft X-rays, it still does not explain how the fan–spine topology was formed in the first place.

These models, although nicely reproducing coronal jets, their associated inverse-Y "Eiffel tower" shape, and the field line geometry obtained from a linear force-free field extrapolation of a jet region (Moreno-Insertis et al. 2008), do therefore not yet provide a satisfying scenario for the formation of anemone active regions. As mentioned above, these regions typically show a ring of bright loops below the jet that is reminiscent of a fan dome, which in some cases might well extend the area of emerged flux.

A two-dimensional effect may also play a role in the brightening of both sides of fan surfaces which form during flux emergence. This effect is the reconnection of emerging field lines back and forth with the ambient fields on both sides of the emerging flux. This is exactly what happens in the 2.5-dimensional simulation of Murray et al. (2009), where an "oscillatory reconnection" pattern (Craig & McClymont 1991) occurs, which the authors attributed to thermal pressure effects around the reconnection layer. This process was also found in 2.5-dimensional simulations of a quadrupolar closed field configuration, being driven by a non line-tied chromospheric adhoc monotonic force (Karpen et al. 1998). Reconnection back and forth was there attributed to coronal relaxation, as a response to an "overshoot" due to a chromospheric driving which was faster in the simulation than on the real Sun. In the simulation of Murray et al. (2009), the photospheric emergence velocities were small compared to the coronal Alfvén speeds (M. J. Murray 2009, private communication), so that such an "overshoot" probably did not occur. However, the existence of (non-wave driven) oscillatory coronal reconnection in fully 3D configurations is yet to be established.

An interesting observational feature of coronal jets is their frequent transverse oscillation (Cirtain et al. 2007). Even though two-dimensional oscillatory reconnection could account for such perturbations (Murray et al. 2009), they could also be caused by non-steady reconnection in a turbulent current sheet, where magnetic islands are gradually formed and destroyed (e.g., Yokoyama & Shibata 1996; Kliem et al. 2000; Archontis et al. 2006), as well as by upward propagating Alfvén waves being launched from the reconnection point (Cirtain et al. 2007; Moreno-Insertis et al. 2008), or by the propagation of a torsional Alfvén wave resulting from the reconnection of kinking twisted field lines with their ambient field (Pariat et al. 2009; Filippov et al. 2009). The latter mechanism provides an explanation also for the frequently observed helical patterns traveling along jets (Shibata et al. 1992b; Patsourakos et al. 2008; Nistico et al. 2009).

In this paper, we propose a fully 3D two-step reconnection model for the formation of broad fan–spine configurations in the corona. The model results from a zero-β line-tied MHD simulation, in which the evolution of the coronal magnetic field is driven by twisted flux emergence prescribed at the photospheric boundary. The simulation was initially developed for the interpretation of a puzzling event observed at the solar limb by the *Hinode* X-ray telescope (XRT). In this event, two distinct small coronal loop systems developed one after the other beside the edge of a prominence cavity, the first one apparently "feeding" the second one, while a swaying jet-like brightening was propagating along the cavity edge. Our model does not only reproduce the shape and timing of the main features observed in this particular event, but also accounts for the formation of full (and not half) anemone bright features, as generally observed in soft X-rays within coronal holes. It finds (in accordance with some past observations and models of coronal jets) that a large fraction of the emerged magnetic twist reconnects and is evacuated upward in the form of a torsional Alfvén wave. It furthermore shows that nullpoint reconnection can be accompanied by slipping reconnection (e.g., Aulanier et al. 2006), which is supported by apparently slipping cavity loops observed by XRT in the event. It finally predicts that a fraction of the twist eventually remains around the inner spine beneath the fan/anemone surface, which therefore does not fully relax to a potential field configuration, even though it looks potential at first order.

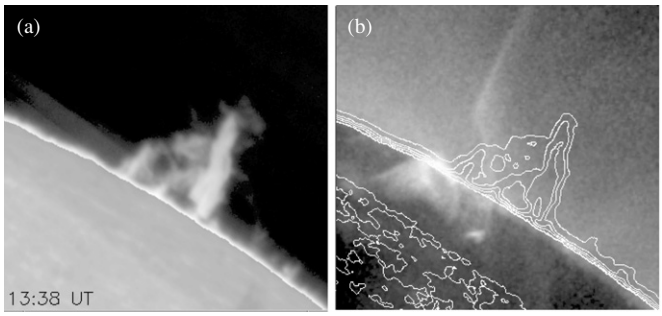

Figure 1. (a) MSDP H_α observation of the prominence on 2007 April 24, at 13:38 UT. (b) XRT observation of the bright loop systems on 2007 April 24, at 18:35 UT (compare with Figure 2), overlaid with H_α intensity contours of (a).

2. OBSERVATIONS

2.1. Instrumentation

The observations presented here were obtained during a coordinated campaign of prominence observations, involving several space and ground-based instruments. They were performed in the JOP 178 frame on 2007 April 23–29, during the first SUMER–*Hinode* observing campaign. JOP 178 has been running successfully many times in the past (see http://bass2000.bagn.obs-mip.fr/jop178/). A prominence surrounded by a cavity on the west limb, at S30 degree, was extensively studied during the campaign (e.g., Heinzel et al. 2008). Figure 1 shows an H_α observation of the prominence obtained by the Multi-channel Subtractive Double Pass spectrograph (MSDP) operating at the Solar Tower of Meudon, as well as an overlay of the corresponding intensity contours with the XRT observations described below. The prominence was located in a quiet Sun region, apparently along the polarity inversion line (PIL) of an extended bipolar area of weak magnetic field, without visible strong field concentrations. A corresponding filament channel could be observed days before in EUV. Here, we focus on XRT observations of a small dynamic event which took place at the edge of the cavity on 24 April.

The *Hinode* mission has been operating since 2006 October (Kosugi et al. 2007). XRT is a high-resolution grazing incidence telescope which consists of X-ray and visible light optics and a 2k $\times$ 2k CCD camera. A set of filters and a broad range of

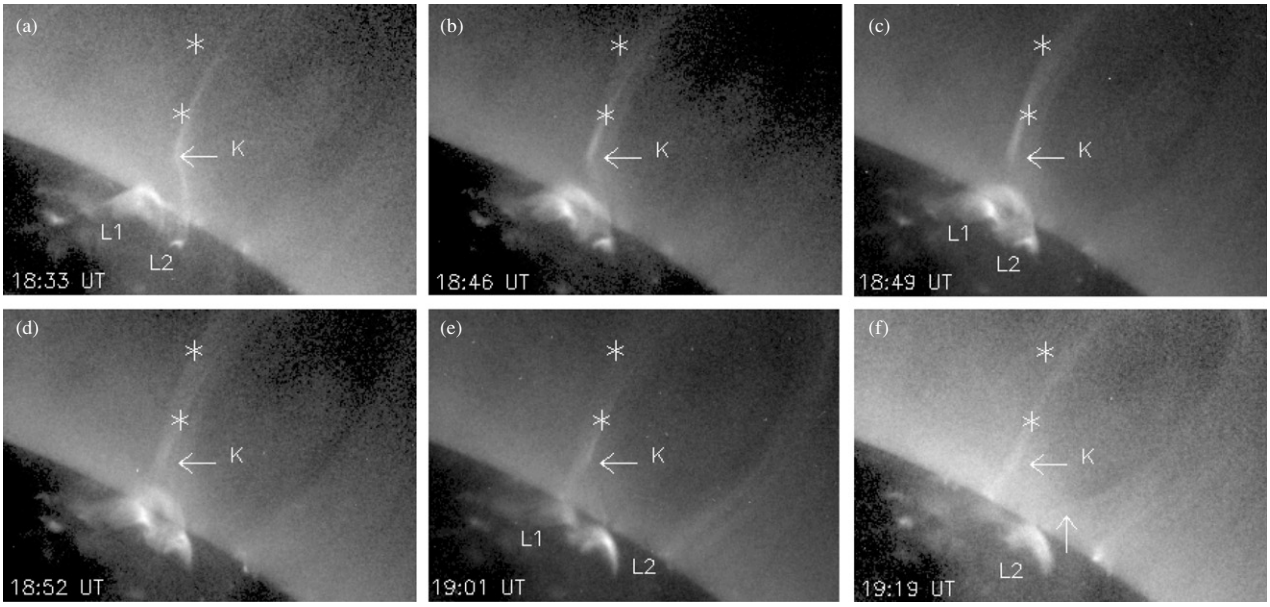

Figure 2. Snapshots from the XRT observations (300″ × 212″) at different times. The bright loop systems are denoted by L1, L2, and K. Asterisks and horizontal arrows are plotted at the same positions in all images to outline the oscillatory transverse motion of K and the displacement of its elbow. The vertical arrow points at loops which are seen to "slip" toward the prominence at the later phase of the evolution. See the text for details. The animation uses a different intensity scaling, which outlines the cavity loops in more clarity.

(An animation of this figure is available in the online journal.)

exposure times enable the telescope to observe hot plasma in the range 10^5–10^8 K (for more details see, Golub et al. 2007). The observations presented here were obtained with a resolution of 512 × 512 pixels, each pixel having a size of 1.″03 × 1.″03. The filter combination used was Al_poly/Open. The exposure time was 8.19 s or 16.38 s, the cadence was 60 s.

2.2. Event Description

The brightening of several loop systems at the edge of the prominence cavity was observed by XRT for about 2 hr on 2007 April 24, between about 18:30 and 20:30 UT. The dynamic evolution described in the following lasted about 45 minutes, ending at 19:15 UT.

Figure 2 shows snapshots outlining the main features of the evolution. At about 18:30 UT, two bright loop systems become visible, one set of small closed loops at the left cavity edge (denoted as L1), and one large loop arching over the prominence (denoted as K), outlining the cavity edge (Figure 2(a)). K exhibits an elbow (indicated by the horizontal arrow), apparently located above L1. A very small loop system is observed at the apparent footpoint of K (denoted as L2 in Figure 2(a)). In the following minutes, L1 continuously grows and the elbow slowly moves to the left. At about 18:39 UT, a brightening begins to propagate along K, starting from below the elbow.

At about 18:45 UT, the evolution becomes more dynamic: L1 seems to expand toward L2, loops apparently connecting L1 and L2 become visible, and L2 starts to grow (Figures 2(b) and (c)). At the same time, the propagating brightening has arrived at the elbow and now moves further along K, exhibiting a jet-like appearance. The upper part of K moves leftward (see asterisks) and after a while the elbow cannot be observed anymore. Shortly after, the part of K on the opposite side of the prominence starts to brighten weakly, indicating that the loop has been filled with hot plasma, ejected from below the elbow (the propagation of the jet-like brightening along K is better visible in the online animation accompanying Figure 2).

At 18:52 UT, L1 and L2 are roughly of the same size. They appear to have a common footpoint region and they collectively exhibit an anemone-like shape (Figures 2(d) and (e)). About this time, the upper part of K moves back toward the right. At 19:01 UT, L1 has started to fade away, and L2 has stopped growing (Figure 2(e)). From about 19:10 UT on, L1 is no longer visible. At 19:19 UT, the upper part of K has returned to its initial position (Figure 2(f)). The transverse oscillatory motion of K is suggestive of an Alfvén wave traveling along it (Cirtain et al. 2007). Between about 19:00 UT and 19:20 UT, a successive leftward displacement of loops starting from the footpoint of K on the opposite edge of the cavity is observed (see the vertical arrow in Figure 2(f)). After that, L2 slowly fades away in about an hour and no further significant dynamic evolution is observed.

The observations suggest that the dynamic evolution was caused by the interaction of newly emerging flux with the arcade-like field overlying the prominence. The inspection of *SOHO*/MDI magnetogram data from the days leading up to the event did not reveal significant long-lived bipolar field concentrations in the vicinity of the prominence, which would have indicated the presence of a 3D nullpoint topology before the event (as in the simulation of Pariat et al. 2009). Since the prominence–cavity system was located at the limb during our event, direct observations of emerging flux are not available. However, the brightening of the elbowed loop system K, as well as the jet-like brightening propagating along it, can be understood by means of models of magnetic reconnection between a small emerging bipole and a predominantly vertical coronal field (see Section 1). This suggests that the loop system L1 was not outlining emerging fields, but rather a reconnected arcade that formed along with the elbow in K. The fact that L1 has a significant height when it becomes visible supports this interpretation. Still, the transverse oscillation of K, the growth of the loop system L2, and the "slipping"-like motion of loops at the opposite edge of the cavity cannot be understood straightforwardly within this scenario.

We note that the observed dynamics did not seem to have a noticeable effect on the stability of the prominence–cavity system. The prominence was still observed on April 25 (Heinzel et al. 2008) and on April 26 by the Meudon Solar Tower. It hence appears that this is a case where emerging flux in the vicinity of a filament or prominence does not result in the eruption of the latter (see, e.g., Feynman & Martin 1995).

3. NUMERICAL SIMULATION

In order to understand the full dynamics observed, we perform a 3D MHD simulation of the interaction of emerging flux with an arcade-like potential field overlying a coronal flux rope. The choice of such a coronal topology is supported by the presence of the prominence–cavity system. Magnetic flux ropes have been successfully used to model prominences and cavities (e.g., Low & Hundhausen 1995; Aulanier & Démoulin 1998; van Ballegooijen 2004; Gibson & Fan 2006). We use the analytical flux rope model by Titov & Démoulin (1999, hereafter TD) as the initial condition in the simulation. The model consists of a toroidal current ring with major radius R and minor radius a, which is partly submerged below a "photosphere" and is held in equilibrium by an external potential field created by two subphotospheric magnetic charges $\pm q$, which are placed at the axis of the torus, at distances $\pm L$ from the current ring. The coronal part of the model yields an arched, line-tied, and twisted flux rope which is embedded into an arcade-like potential field (see Figure 2 in TD). The depth d of the torus axis (and hence of the magnetic charges) below the photospheric layer determines the compactness and strength of the magnetic flux distribution in the photospheric plane. Here, we choose a relatively large depth (see below), in order to account for the observed extended area of weak field above which the prominence was located (see Section 2.1).

Previous simulations (Török et al. 2004; Török & Kliem 2005, 2007; Schrijver et al. 2008) and analytical calculations (Isenberg & Forbes 2007) have shown that the TD flux rope can be subject to the ideal MHD helical kink and torus instabilities. Therefore, we use a weakly twisted rope here, with the field lines winding on average only once about the rope axis (in a right-handed sense), and we choose the potential field such that the rope is stable with respect to the torus instability (Bateman 1978; Kliem & Török 2006).

As in these previous simulations, we integrate the $\beta = 0$ compressible ideal MHD equations:

$$\partial_t \rho = -\nabla \cdot (\rho \boldsymbol{u}), \tag{1}$$

$$\rho\, \partial_t \boldsymbol{u} = -\rho(\boldsymbol{u} \cdot \nabla)\boldsymbol{u} + \boldsymbol{j} \times \boldsymbol{B} + \nabla \cdot \mathbf{T}, \tag{2}$$

$$\partial_t \boldsymbol{B} = \nabla \times (\boldsymbol{u} \times \boldsymbol{B}), \tag{3}$$

where $\boldsymbol{B}$, $\boldsymbol{u}$, and ρ are the magnetic field, velocity, and mass density, respectively. The current density is given by $\boldsymbol{j} = \mu_0^{-1} \nabla \times \boldsymbol{B}$. The term $\mathbf{T}$ is the viscous stress tensor, included to improve the numerical stability (Török & Kliem 2003). We neglect thermal pressure and gravity since we are interested in the qualitative evolution of the magnetic field only.

The MHD equations are normalized by quantities derived from a characteristic length, taken here to be the initial apex height of the TD flux rope axis above the photospheric plane, $R - d$, the initial magnetic field strength, B_0, and Alfvén velocity, v_{a0}, at the apex of the axis, and derived quantities. We use a nonuniform cartesian grid of size $[-4, 4] \times [-5, 5] \times [0, 8]$, resolved by $261 \times 301 \times 208$ grid points (including two layers of ghost points in each direction which are used to implement the boundary conditions), with a resolution of $\Delta x = \Delta y = 2\Delta z = 0.02$ in the box center. The resolution is nearly constant in the subdomain $[-1, 1] \times [-1.5, 1.5] \times [0, 1]$, and increases exponentially toward the boundaries, to maximum values $\Delta x_{\max} = 0.14$, $\Delta y_{\max} = 0.10$, and $\Delta z_{\max} = 0.40$. The plane $\{z = 0\}$ corresponds to the photosphere.

The TD flux rope axis is oriented along the y-direction, with the positive polarity rope footpoint rooted in the half-plane $\{y > 0\}$ (see Figure 3). The normalized geometrical flux rope parameters used are: $R = 2.75$, $a = 1.$, $L = 2.5$, and $d = 1.75$. The top left panel in Figure 3 essentially shows the initial TD configuration, except for the small parasitic bipole and the blue field lines on the left-hand side of the TD flux rope.

We employ a modified two-step Lax–Wendroff method for the integration, and we additionally stabilize the calculation by artificial smoothing of all integration variables (see Sato & Hayashi 1979; Török & Kliem 2003, for details). The reconnection occurring in our simulation is due to the resulting numerical diffusion. The initial density distribution is $\rho_0(z) = 2.6 \exp(-[z + \Delta z]/1.1)$, chosen such that the Alfvén velocity, v_a, slowly decreases with height above the TD flux rope. The system is at rest at $t = 0$.

We first perform a numerical relaxation of the system for 37 Alfvén times and reset the time to zero afterwards. We then model the emergence of a second twisted flux rope in the vicinity of the TD rope, following the boundary-driven method by Fan & Gibson (2003, hereafter FG). In their model, a toroidal twisted flux rope is rigidly emerged from a fictitious solar interior into a coronal magnetic field by successively changing the boundary conditions in the photospheric layer of the simulation box. We refer to Figure 1 in FG for a sketch of the model. In our simulation, we choose the FG torus to be about 1 order of magnitude smaller in size than the TD torus (the major and minor radius of the FG torus are 0.3 and 0.2, respectively), in order to account (within the limitations given by the finite number of grid points) for the typically large difference in size between quiescent filaments and small bipoles that emerge in their vicinity (see, e.g., Feynman & Martin 1995), which was also suggested by the relative scale lengths of the coronal loops observed in the event described in Section 2.2.

The FG flux rope is uniformly twisted along its cross section. The twist is chosen right handed, with the field lines winding ~4.5 times along the whole torus. We position the rope such that the emergence region is centered at $(x, y) = (-1.0, -0.5)$, within the large-scale negative polarity of the TD potential field. As the TD flux rope, it is oriented along the y-direction, but with the opposite orientation of the axial magnetic field (see Figure 3). The magnetic field strength within the FG torus varies along its cross section, being $\sim 3\, B_0$ at the outer torus surface, $4 B_0$ at the axis, and $\sim 13 B_0$ at the inner torus surface, for the parameters used in the simulation. Although the emergence is driven until the apex of the inner surface approaches the bottom boundary of the box (see below), the field strength which effectively enters the corona during the simulation does typically not become larger than $\sim 6 B_0$. The field strength of the large-scale TD field in the small volume above the emergence area is approximately constant, $\sim 0.7\, B_0$. Within the TD flux rope, the field strengths vary between ~0.6 and $1.0\, B_0$. We discuss the rationale for our choice of the orientation and strength of the magnetic field within the FG flux rope in Section 5.

The boundary-driven emergence is imposed in the layer $\{z = -\Delta z\}$. Within the emergence area in this layer, we overwrite the pre-existing TD field by the respective FG flux

rope field, and we set the vertical velocity equal to the respective driving velocity, while keeping the horizontal velocities at zero. Outside this area, the TD field and the density in $\{z = -\Delta z\}$ are kept at their initial values, and the velocities are set to zero, at all times. These settings lead to significant jumps in strength and orientation of the magnetic field (i.e., to the formation of large values of $\nabla \cdot \mathbf{B}$) at the interface between the TD and FG fields at and close to the bottom plane. Since our code does not conserve $\nabla \cdot \mathbf{B} = \mathbf{0}$ to rounding error, we use a diffusive $\nabla \cdot \mathbf{B}$ cleaner (Keppens et al. 2003), as well as Powell's source term method (Gombosi et al. 1994), to minimize unphysical effects resulting from $\nabla \cdot \mathbf{B}$ errors. Furthermore, our overspecified boundary conditions (see above) trigger spurious oscillations, which after some time lead to numerical instabilities close to the bottom plane, in particular at the interface between the TD and FG fields. In order to prevent these instabilities, we apply an enhanced smoothing of all variables close to the boundary (as in Török & Kliem 2003), and we set the Lorentz force densities at $\{z = 0\}$ to zero at all times. We find that these settings result in the formation of a rising twisted flux tube above the emergence area, as desired.

The emergence is driven quasi-statically with a maximum velocity of $0.01 v_{a0}$. The driving velocity is linearly increased and decreased for 10 Alfvén times before and after the main emergence phase (which lasts for 30 Alfvén times), respectively. The emergence is stopped at $t = 50$, when the apex of the inner surface of the FG torus has reached the layer $\{z = -\Delta z\}$. The total twist transported into the corona by the emerged section of the FG torus corresponds to $\sim$1.7 field line turns.

4. SIMULATION RESULTS AND COMPARISON WITH XRT OBSERVATIONS

In this section, we describe our simulation results and compare them with the XRT observations described in Section 2.2. The interaction between the emerging FG flux rope and the pre-existing TD coronal field results in two distinct reconnection phases, which are described in Sections 4.1 and 4.2, respectively. In Section 4.3, we discuss the magnetic field geometry resulting from the reconnections, and in Section 4.4 we describe the response of the TD flux rope and its surrounding arcade to the dynamics accompanying the reconnection. In order to emphasize that the evolution found in the simulation does not rely on the specific flux rope models used, we refer to the FG rope as "emerging flux rope," and to the TD rope as "prominence flux rope" throughout this section.

Figures 3–5 display magnetic field lines which outline the main features of the magnetic field evolution in the coronal domain. Figures 3 and 4 focus on the dynamics, showing the first and second reconnection phase, respectively. Figure 5 shows the evolution of the magnetic topology. The blue field lines in Figures 3–5 are integrated starting from the negative polarity of the emerging flux rope, green field lines in Figures 3 and 4 outline the core of the prominence flux rope (black circles mark field line dips). Red (pink) field lines in Figures 3 and 4 show the outer (inner) arcade overlying the prominence flux rope initially, and reconnected field lines later on. Note that all field lines are calculated from the same positions on the left-hand side of the prominence flux rope in all panels.

4.1. First Step: Formation of One-half of the Anemone and Jet Acceleration

As the emerging flux rope (closed blue field lines in the bottom panels of Figure 3) enters the coronal domain, it starts to expand and a current sheet forms above the outer edge of its positive polarity, at the interface of the rope and the outer coronal arcade that surrounds the prominence flux rope. Since the outermost emerging fields and the outer arcade fields are oppositely directed at the location of the current sheet, the two flux systems readily start to reconnect, forming a new small loop system below the current sheet and strongly bent, elbow-shaped field lines above it (cusp-shaped red field lines and blue field lines in the central panels of Figure 3, respectively). Note that the not yet reconnected part of the emerging flux rope continues to expand in the corona after the reconnection has started. The shape of the reconnected field lines agrees very well with the shape of the bright loops observed by XRT in the early phase of the event described in Section 2.2 (see L1 and K in Figure 2(a)), which indicates that the observed loops have been formed in an analogous reconnection process.

The field line shapes are a signature of a fan–spine configuration in a 3D nullpoint topology (see also Figure 5(b)). A magnetic nullpoint is indeed formed within the current sheet in the simulation, right after the reconnection has started. It forms as the system tends to relax to a lower energy state.[3] The reconnection continues as time evolves, thus the size of the reconnected red loop system increases (Figure 3), in agreement with the observed growth of L1 (Figures 2(a) and (b)). The ongoing expansion of the emerging flux rope initially slowly pushes the nullpoint away from the prominence flux rope, in agreement with the observed leftward displacement of the elbow indicated by the horizontal arrow in Figure 2.

As the emergence continues, the emerging flux rope field lines become increasingly sheared with respect to the surrounding coronal arcade. This is due to the fact that the twist within the FG flux rope is nearly uniform along its cross section (as in the well-known Gold–Hoyle model). While field lines far away from the flux rope axis are strongly inclined with respect to the axis, field lines close to the axis are almost aligned with it. Hence, as the flux rope emerges, its outer field lines resemble a nearly potential coronal arcade that is oriented almost orthogonal to the local PIL, whereas its inner field lines (i.e., those close to its axis) resemble a small sheared coronal arcade (see Figure 6). The first flux rope field lines which reconnect with the large-scale coronal arcade are thus almost unsheared with respect to the arcade (see the bottom left panel in Figure 3). As the evolution continues, progressively more sheared loops are reconnected. As a result, the system of new reconnected (red) field lines eventually develops a shear distribution that is opposite to the one of the emerging flux rope: the field lines are sheared at the edges of the system, and almost unsheared close to the local PIL (see the bottom right panel in Figure 3 and the corresponding online animations).

The reconnection does not only yield the transfer of twist from the emerging flux rope into the newly formed red loop system. Part of the flux rope twist is also transferred into the lower parts of the reconnected overlying blue field lines that are now rooted in the negative polarity of the rope. Since the upper parts of these field lines are nearly potential, whereas their lower parts experience a sudden injection of twist, they are far from being force free. Their relaxation is ensured through the launch of a torsional Alfvén wave which travels from low altitudes all

[3] The lowest possible energy state for any photospheric magnetic field distribution which develops during the emergence process would locally (i.e., above the emergence region) correspond to a potential field that has to contain one single nullpoint, owing to the presence of a closed PIL embedded in a region of nearly vertical field (e.g., Antiochos 1998, see Introduction).

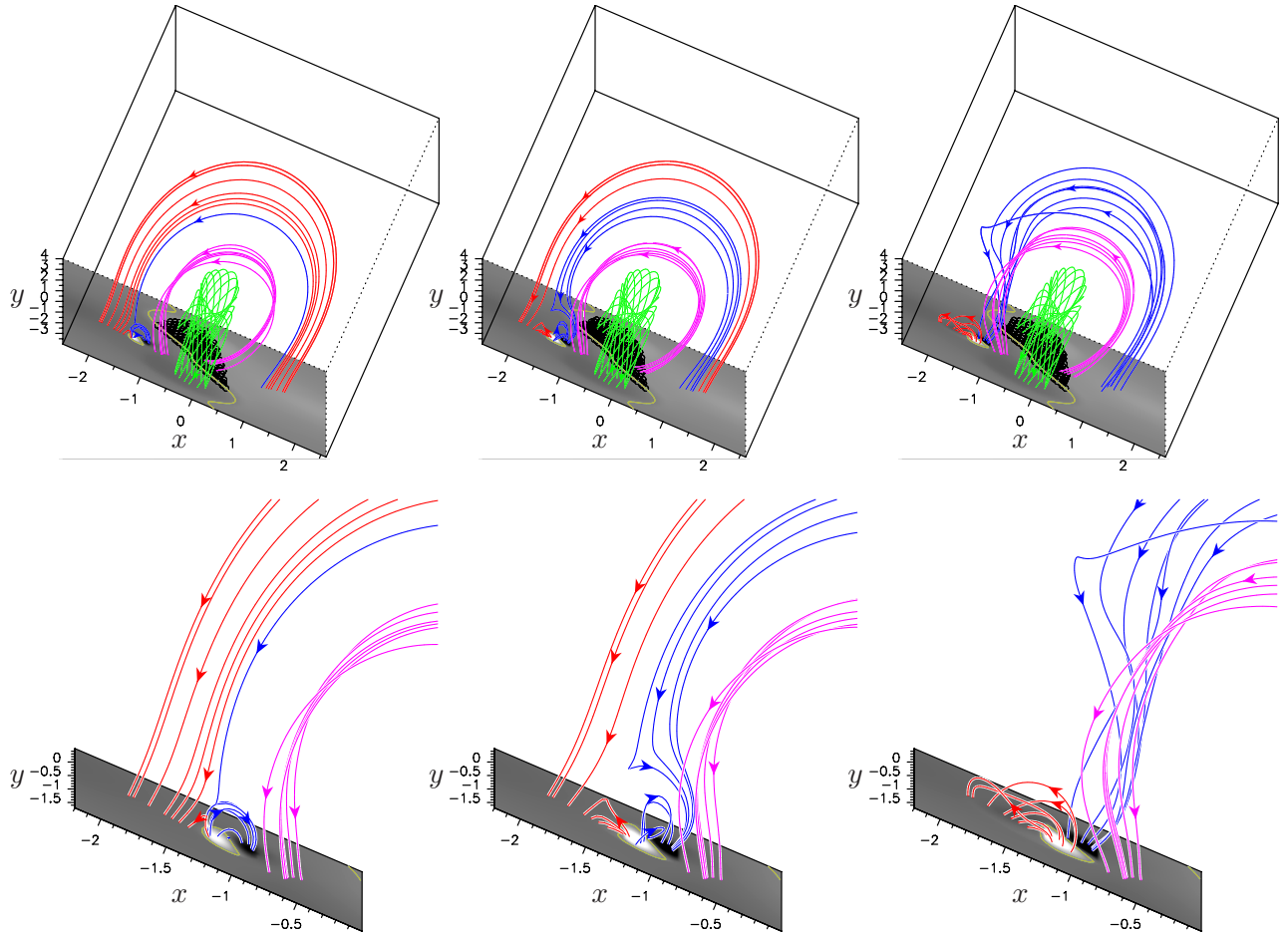

Figure 3. Selected magnetic field lines outlining the first reconnection which occurs between the emerging flux rope and the outer coronal arcade. The bottom panels show a zoom into the emergence region. Contours of $B_z > 0$ ($B_z < 0$) at the bottom plane $\{z = 0\}$ are shown in white (black). Polarity inversion lines (PILs) are drawn in yellow. The negative polarity of the large-scale potential field is located on the left-hand side of the main PIL. All field lines are calculated from fixed footpoints on the left-hand side of the main PIL in all panels. From left to right: at onset of ($t = 22$), during ($t = 34$), and after ($t = 43$) the reconnection. Blue field lines the negative polarity of the emerging flux rope, green field lines show the core of the prominence flux rope. Red field lines outline the outer coronal arcade at early times and the newly formed small loop system later on. Pink field lines show the inner coronal arcade. Arrowheads mark the direction of the magnetic field. The black circles located above the main PIL mark field line dips, which are assumed to carry prominence material.

(Animations [A, B] of this figure are available in the online journal.)

along the arcade (see the evolution of the blue field lines in Figures 3 and 4).

Such reconnection between twisted and untwisted coronal fields has been suggested by several authors as a driving mechanism for jets (see, e.g., Schmieder et al. 1995; Shibata et al. 1997). If the reconnection is sufficiently impulsive, it can launch a shear (in 2.5D) or torsional (in 3D) Alfvén wave, which can accelerate the plasma upward, as shown in numerical simulations by Yokoyama & Shibata (1999) and Pariat et al. (2009), respectively. The impulsive nature and large wavenumber of the wave in our simulation is a priori not expected, since the transition from nearly unsheared to highly sheared emerging flux rope fields lines involved in the reconnection is continuous. Also, our code does not incorporate any time-varying resistivity. Therefore, the impulsive launch of the wave must result from some perturbation of the system which yields a strong increase of the reconnection rate. Indeed, we find a strong expansion of the not yet reconnected central part of the emerging flux rope at $t \approx 40$ (i.e., between the stages shown in the middle and right panels of Figure 3; see the corresponding online animation). At this time, a flux rope twist of $\sim$1.5 turns has entered the corona, indicating that this sudden increase in expansion might be related to the onset of a kink instability (as in Fan & Gibson 2003, 2007). The reconnection-driven torsional Alfvén wave in our simulation suggests an explanation for the jet-like brightening traveling along the cavity loops observed by XRT in our event, as well as for the observed transverse oscillation of the upper parts of the cavity loops (see Section 2.2).

The transverse deformation of the blue field lines in our simulation during the passage of the wave (Figure 4) is, however, obviously much larger than what is observed in our event and typically in coronal jet-like events (Cirtain et al. 2007). This might simply be due to the fact that, although we have chosen the emerging flux rope to be as small as possible as compared to the prominence flux rope (see Section 3), the difference in size between the emerging flux and the prominence–cavity system might still be significantly larger. Also, to some extent the unrealistic reconnection timescales in our simulation might play a role. They are mostly constrained by the intrinsic diffusivity of the numerical scheme and by the prescribed magnetic field smoothing, and do neither correspond to fast reconnection nor to the seminal Sweet–Parker regime. Still, the qualitative agreement which we find here with other coronal

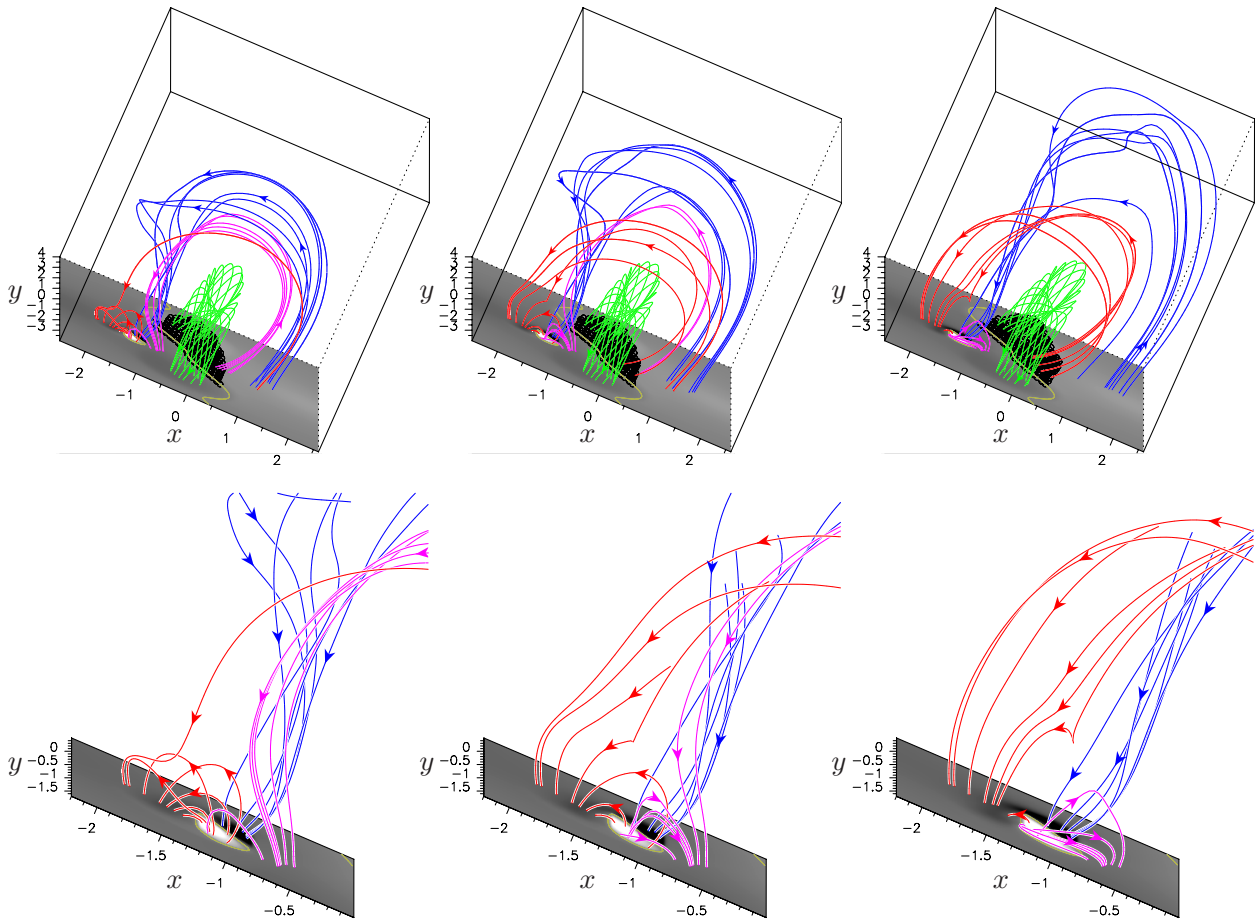

Figure 4. Snapshots of the configuration outlining the second reconnection, which occurs between the newly formed small loop system and the inner coronal arcade. Field lines, contours, and black circles are as in Figure 3. The bottom panels show a zoom into the emergence region. From left to right: at onset of ($t = 46$) and during ($t = 49, 57$) the reconnection. Pink field lines show the inner arcade initially, and the second newly formed loop system later on. The propagation of an Alfvén wave along the blue field lines and the slipping motion of the footpoints of the red field lines on the right-hand side of the prominence flux rope are visible.

(Animations [A, B] of this figure are available in the online journal.)

jets simulations performed with different codes (see Section 1) suggests that we can believe in the overall mechanism for jet acceleration which our simulation finds.

Note that the nullpoint-related elbow in the lower part of the blue field lines apparently disappears during the evolution in our simulation (as it does in the observation too; see Figure 2). In the simulation, this is merely due to projection effects and the motion of the nullpoint. From a different viewing angle, an elbow at low heights remains visible.

Up to this point, the evolution is as expected from the classical model for coronal jets and previous 2.5D and 3D simulations of this model (see Section 1 and Figures 5(a) and (b)). It results in the formation of a 3D nullpoint topology, but actually half of its fan surface still consists of not reconnected emerged field lines, so that only the other half is expected to brighten in soft X-rays. In other words, only a *half* anemone has been formed at this stage in the simulation.

4.2. Second Step: Formation of the Second Half of the Anemone

As the reconnection-driven transfer of twist/shear from the emerging flux rope into the ambient coronal field progresses, the footpoints of the newly formed red field lines located within the positive polarity of the emerging flux rope are continuously displaced in the negative y-direction (see Figure 3 and the online animation), toward inner arcade field lines which also overlie the prominence flux rope and are yet unaffected by the reconnection (shown in pink in Figure 3). Meanwhile, following the magnetic field reorientation at high altitude, the nullpoint (and hence the reconnection site) undergoes a counterclockwise horizontal rotation, from the leftmost edge of the emerging rope toward its center, thereby approaching the pink arcade field lines (see Figure 5). The displacement of the footpoints of the small red loop system corresponds to the apparent expansion of L1 toward L2 in the observation, which starts at about 18:45 UT (see Section 2.2).

Eventually, a second reconnection starts, now between the previously reconnected sheared red field lines and the pink arcade field lines (Figure 4). It must, and indeed does, take place at the nullpoint, which has gradually moved toward the pink arcade during the first reconnection episode (see above). This second reconnection leads to the formation and growth of a second small loop system (cusp-shaped pink field lines in Figure 4), which corresponds to the growth of the observed bright loop system L2 from about 18:50 UT on (Figure 2). The reconnected red and pink loop systems both have footpoints within the positive polarity of the emerging flux, and they collectively display an anemone-like shape which is significantly wider than this polarity (Figure 5(c); compare also with the collective shape of L1 and L2 in Figures 2(d) and (e)).

In the course of the second reconnection, the sheared red loop system "feeds" the newly formed small pink loop system with magnetic flux, hence the former shrinks while the latter grows

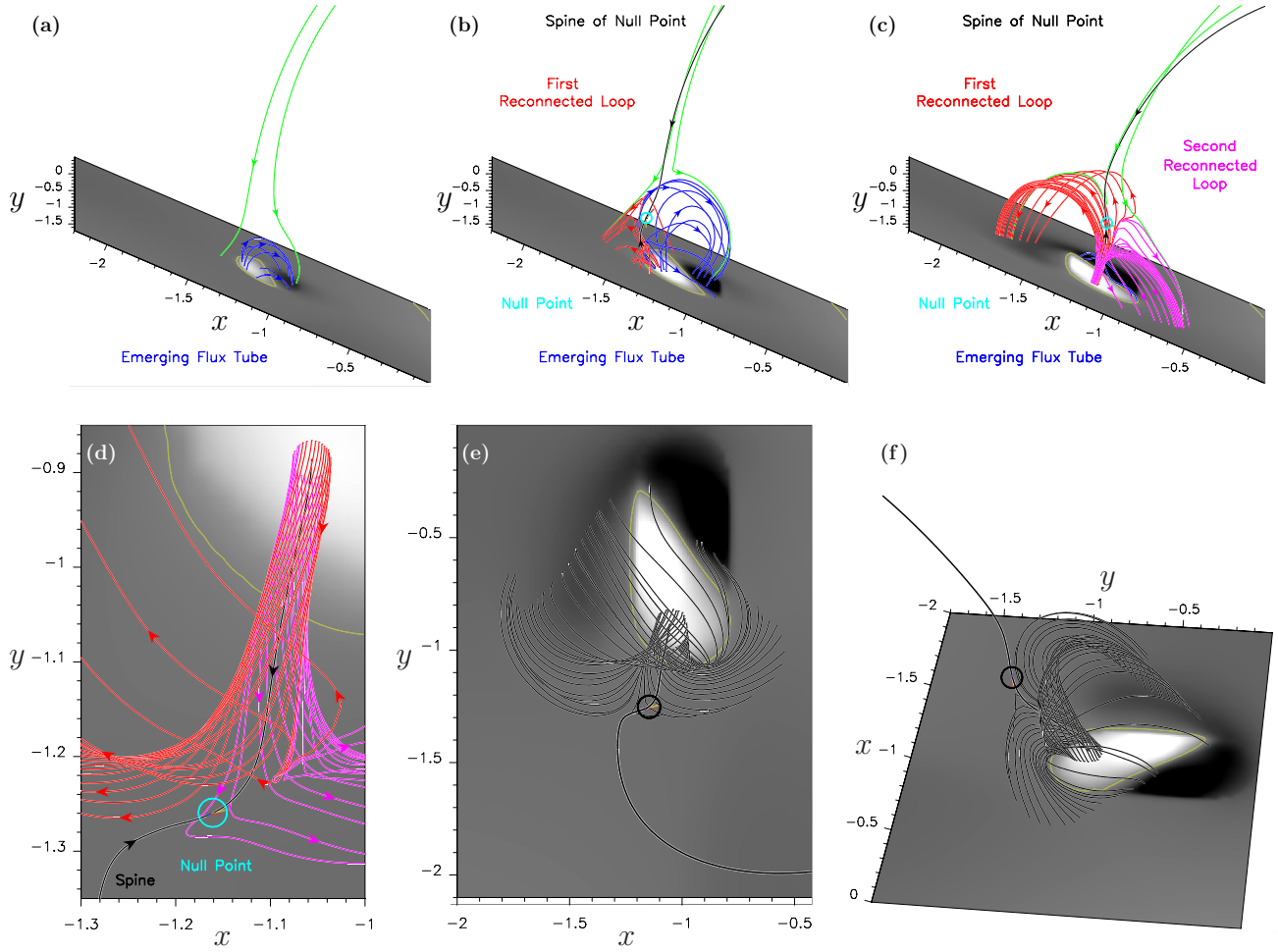

Figure 5. (a–c) Side view on the flux emergence region in the simulation at $t = 17$, 34, and 51. The contours at the bottom plane are as in Figures 3 and 4. Selected magnetic field lines are shown in order to outline the topological evolution. (d) Top view on the center of the anemone-shaped loop pattern shown in (c), outlining the twist of the field lines. (e and f) Top and side view on the emergence region at $t = 51$, showing field lines starting from a circle around the spine (black line) with twice the radius as used in (c) and (d). These field lines approximately outline the fan surface. The respective positions of the nullpoint are indicated by circles.

(Figure 4). Although, at first glance, the bottom right panel gives the impression that the red loop system has almost disappeared, the elbow visible in the rightmost red arcade field line shows that there still exist relatively extended, not reconnected red loop field lines at this late phase of the second reconnection. These field lines are rooted between the elbow-shaped field line and the rightmost, very flat red field line. The final relative size of the red and pink loop systems will depend on how long reconnection persists, which, in turn, will depend on a number of factors, as for example on the ratio of the respective magnetic fluxes present in the reconnecting flux systems and on the lowest state of magnetic energy the system can reach by means of its relaxation. A shrinking of L1 during the growth of L2 is also indicated by the observations (compare Figures 2(d) and (e)). However, this "shrinking" might be merely due to a relatively fast cooling of L1. Studying the issues of lifetime and visibility in soft X-ray of the reconnected loops in our simulation would require the inclusion of proper thermodynamics, which is beyond the scope of this paper.

4.3. Geometrical Properties of the Reconnected Field

The geometrical properties of these new loop systems in the simulation are different from what has been found in the simulations mentioned in Section 1. They arise from a two-step and fully 3D transfer of sheared flux, first from the sheared core of the emerging flux rope into the new small loop system formed at its side (as the emerging blue field lines reconnect with ambient [red] arcade field lines that are anchored on the left-hand side of the emerging rope), and second from the very same loop system into a second generation of small loops, which form at the other side of the emerging flux rope (as the sheared small red field lines reconnect with other ambient (pink) arcade field lines).

As a result, a *full* anemone forms around the parasitic polarity of the emerging bipole. A large fraction of the nullpoint associated fan now consists of once or twice reconnected field lines, and not to a large extent of emerged field lines as in most of the models described in Section 1. Since both sides of the fan have been formed through magnetic reconnection, they can a priori be both visible as hot loops in soft X-rays. The center of the anemone structure contains significant twist once it has fully formed, although the structure appears to be potential when viewed from some distance (Figure 5(c)). The twist is concentrated around the inner spine of the nullpoint (see Figure 5(d)), but some of it is also present along the fan. This twist is the remnant of magnetic shear that has not been ejected in the form of a torsional Alfvén wave along the large-scale reconnected arcades that overlie the prominence flux rope.

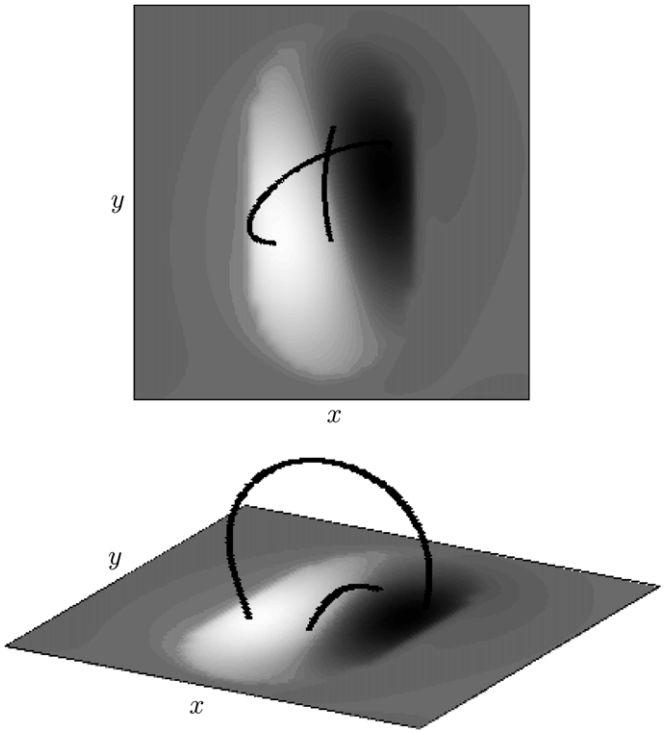

Figure 6. Top and oblique view on two field lines within the emerging flux rope at $t = 31$, outlining the change of field line inclination during the emergence. See the text for details.

It is worth noting that, even though a fully 3D anemone has been formed, it still locally possesses a quasi, but not exact, translational invariance along the *y*-axis, i.e., along the axis of the emerging flux rope, around the nullpoint. This can be seen in Figures 5(c)and (d): almost all of the red and pink field lines fan out roughly along the *x*-direction, i.e., perpendicular to the rope axis, even though they have been integrated from equidistant footpoint positions along a small circle centered at the inner spine of the nullpoint, within the positive polarity of the emerging flux, where B_z is roughly constant (as shown in Figure 5(d)). This strong departure from axisymmetry around the nullpoint, which does not exist in all of the 3D nullpoint models (e.g., Antiochos 1998; Pariat et al. 2009), can here be attributed to the elongation of the emerging flux, and possibly to the different inclinations of the ambient field lines. The few red and pink field lines in Figure 5(d) which fan out from the nullpoint region along the positive *y*-direction, clearly show that the anemone does not contain a true null line, but one single nullpoint. The quasi-translational invariance is then due to fan-related eigenvalues of the single nullpoint, which have very different amplitudes (Lau & Finn 1990). This property, which has already been identified in the simulation of Masson et al. (2009) with a different MHD code, may be present also in other simulations, such as those which let emerge a very long flux rope (e.g., Moreno-Insertis et al. 2008).

Figure 5(e) and (f) show that, despite the strong departure from axisymmetry, the fan surface also extends in the *y*-direction, i.e., along the axis of the emerging flux rope. The field lines shown in the two panels are located very close to the fan surface and outline a "heart-shaped" form of the fan. We expect the fan to develop a more uniform radial distribution as the system relaxes to a force-free field, or if less elongated parasitic polarities are considered (Antiochos 1998).

4.4. Response of the Prominence Cavity to the Anemone/Jet Formation

While the two-step reconnection described in the previous subsections persists beside the prominence flux rope, the torsional Alfvén wave triggered during the first reconnection phase travels upward (see the evolution of the blue field lines in the top panels of Figure 4). Even though the upper part of the prominence flux rope significantly bends to the side while the wave passes by, the simulated "prominence material" located in the flux rope dips (computed as in Aulanier & Démoulin 1998; van Ballegooijen 2004; Gibson & Fan 2006; Dudík et al. 2008; and indicated by the black circles in Figures 3 and 4) does not show a significant motion. This difference is due to the relatively small twist of the rope combined with its non-negligible curvature, which result in the occurrence of magnetic dips only far below the rope axis, at altitudes low enough not to be significantly affected by the wave (see also the discussion on the strength of the perturbation caused by the wave in Section 4.1).

A perturbation of the cavity is observed by XRT on the right-hand side of the prominence in our event. Between 19:01 and 19:19 UT, after the formation of L1, while the jet-like brightening is still propagating and L2 is still growing, a continuous motion ("slipping") of the lowermost parts of several loops, from the outer edge of the cavity toward the prominence, becomes visible (see Figure 2(e), Figure 2(f), and the corresponding XRT movie). Estimating their slipping velocities by following them individually is not straightforward, as all these loops are not very much contrasted with respect to the background corona. The only sure number we could derive is a minimum drift velocity of $35\,\mathrm{km\,s^{-1}}$ for the ensemble of these loops, since they all have moved by $51''$ along the solar limb during a time interval of 18 minutes. Still, we cannot rule out that the drift velocity of individual loops could be much larger.

The very same phenomenon takes place in the simulation. The online animation of the simulation shows a slipping motion of the footpoints of the red large-scale arcade field lines on the right-hand side of the prominence flux rope (see also the top panels in Figure 4). This slipping occurs along the footpoints of arcade field lines (of which some are shown by the pink field lines in the left panels of Figure 4). It starts right after the second reconnection sets in and begins to exchange the connectivities between the small (and already once reconnected) sheared red field lines and large-scale arcade field lines. This slipping of field lines, after they have reconnected at the nullpoint, is not a numerical artifact, caused by insufficient accuracy of the field line integration or by a too strong smoothing of the magnetic field during the MHD simulation: the slipping occurs over many grid points in the large-scale positive polarity beside the prominence flux rope, and it does not occur outside of flux regions which reconnect at the nullpoint. A very mild slipping is noticeable also during the first reconnection, at the footpoints of the reconnected large-scale blue lines along which the wave travels (see the online animations corresponding to Figures 3 and 4).

The explanation of this slipping is very probably the same as first put forward by Masson et al. (2009) in their nullpoint associated confined flare model: the asymmetry of the fan–spine configuration, manifesting as a local quasi-translational invariance of the magnetic field around a nullpoint, which has one fan-related eigenvalue of very small, but finite value (see Section 4.2 and Figures 5(c) and (d)), results in the appearance

of a narrow halo of finite width around the nullpoint separatrices, in which field lines have strong squashing degrees, i.e., which constitutes quasi-separatrix layers (QSLs; Démoulin et al. 1996). It has been recently shown that current sheet formation and diffusion at QSLs result in slipping/slip-running magnetic reconnection, manifesting as apparent field line motions at sub/super Alfvénic speeds (Aulanier et al. 2005, 2006). In the case of a 3D nullpoint topology, the presence of a QSL halo surrounding both the fan surface and the spine field line results in a complex pattern for magnetic reconnection, in which a given field line slips and slip-runs, both before and after its connectivity jumps at the nullpoint. To the best of our knowledge, the present simulation is the second one after Masson et al. (2009) for which this sequential nullpoint and slipping reconnection behavior is reported. Based on these simulations, the slipping loops observed by XRT in our event can be regarded as a new direct evidence for slipping reconnection in the corona, as previously observed by Aulanier et al. (2007).

5. DISCUSSION

We presented a $\beta = 0$ 3D MHD simulation of the interaction of a small emerging bipole with a large-scale arcade-like coronal field overlying a weakly twisted coronal flux rope. The simulation was developed in order to understand *Hinode*/XRT observations of a small limb event which took place at the edge of a quiet Sun prominence cavity. The event showed a number of puzzling features, which could satisfactorily be explained by the magnetic field evolution in the simulation (see Section 4 for details).

The main results of the simulation can be summarized as follows.

1. The emergence of a twisted flux rope into one large-scale polarity of an arcade-like coronal field yields the formation of a fully 3D single nullpoint topology in the corona, consisting of a fan–spine configuration in which the fan surface *significantly extends* over the parasitic polarity of the emerged flux.
2. The configuration forms in a *two-step reconnection* process at the nullpoint, which yields the successive formation of two small loop systems below the fan surface, on opposing sides of the parasitic polarity. The first loop system hereby "feeds" the second one with magnetic flux. Since the two loop systems (and field lines surrounding them) have common footpoints in the parasitic polarity, they collectively display an *anemone* shape.
3. The reconnection facilitates the transfer of twist/shear from the emerging flux rope into the coronal arcades by means of a *torsional Alfvén wave* which travels along the arcades. A fraction of the twist remains below the fan surface, where therefore the resulting magnetic field is nonpotential.
4. The wave is launched by reconnection, as the expansion velocities of the emerging fields in the corona suddenly increase, possibly due to the onset of a ideal MHD kink instability in the not yet reconnected part of the emerging flux rope, after sufficient twist has entered the corona.
5. The 3D nullpoint reconnection is accompanied by *slipping reconnection* of arcade field lines on the opposite side of the pre-existing coronal flux rope. This can probably be explained by the presence of quasi-separatrix layers around the nullpoint.

Our simulation combines dynamic and topological elements of flux emergence into unipolar coronal fields and coronal jet formation which have previously not been found altogether in a single simulation. The two-step reconnection process found in our simulation provides a new model for the formation of 3D nullpoint topologies with extended fan surfaces in the corona. By means of reconnection between twisted and untwisted fields, the model can also account for coronal jet activity (e.g., Schmieder et al. 1995; Shibata et al. 1997; Pariat et al. 2009). Finally, since the fields below the fan surface are all formed by reconnection, and can therefore a priori assumed to brighten in soft X-rays, our simulation also suggests a mechanism for the formation of (full) anemone active regions. The fact that some of the emerging twist remains below the fan surface in the final configuration supports models of jet formation which assume a twisted null point configuration prior to the jet (e.g., Pariat et al. 2009).

Our model can, however, not account for the *long-lived evolution* of anemone active regions. Such regions are observed to consist of bright loops on both sides of a parasitic polarity over time-periods of days (e.g., Asai et al. 2008), whereas the reconnection in our simulation is expected to produce rather short-lived brightenings, which would occur successively rather than simultaneously (as in the event described in this paper). It seems likely that the long-lived dynamics of anemone regions is due to continuous dynamic perturbations of the configuration after its formation by, for instance, ongoing flux emergence and photospheric flows. Our model might serve as a starting point for a numerical study of anemone region dynamics.

Let us now briefly discuss the robustness of our results with respect to the variation of various model parameters. A detailed investigation of this question will require an extensive parametric study, but some aspects may be discussed here.

First of all, the model relies on fully 3D effects. The most important ingredient is the twist brought up by the emerging flux rope. For the two-step reconnection as described in this paper to work, the emerging field lines must significantly change their inclination as they rise into the corona, such that the first reconnected loop system can evolve toward yet unreconnected remote ambient fields during the reconnection. If the twist in the emerging flux rope (more precisely: the change of field line inclination along the cross-section of the rope) is chosen too small, the first reconnection will occur (as in the flux emergence simulations mentioned in Section 1), but the second one will not set in. Our adopted boundary-driven "kinematic" flux emergence technique models the rigid emergence of a twisted flux rope into the corona, and does therefore not capture the dynamics of real flux emergence (for a discussion, see Fan & Gibson 2003). In particular, it assures that the inclination of the emerging field lines is continuously changing. It would be, of course, desirable to test our model in a "dynamic" flux emergence simulation, as the one by Moreno-Insertis et al. (2008). Here, we have chosen the "kinematic" approach since, at present, "dynamic" flux emergence simulations do not allow to consider complex coronal magnetic field configurations as the one used here, which was chosen to model the observed prominence–cavity system.

Apart from the twist profile of the emerging flux rope, there are several other model parameters which had to be chosen carefully in order to match the observations (but not necessarily to produce a 3D nullpoint configuration, which is more general). First, of course, the size of the emerging flux rope and its distance from the coronal flux rope had to be adjusted as suggested by the observations. Second, the choice of the magnetic field strength within the emerging rope (and therefore its magnetic flux) is important. The ratio of the field strength (and flux) between

the emerging rope and the ambient corona will influence, for instance, the amplitude of the torsional Alfvén wave and the final size of the reconnected small loops, i.e., the size of the anemone. In the simulation presented here, the field strength within the coronal part of the emerging flux rope was typically about five times larger than in the neighboring arcade fields throughout most of the evolution, so that the flux within the (small) rope was not negligible compared to the flux contained in the large-scale arcades. Third, the inclination of the initial coronal field might play a role, although we expect a similar evolution if the flux rope would be emerged into a purely vertical coronal field, mimicking "open" field lines in coronal holes. Finally, the magnetic orientation of the emerging rope with respect to the pre-existing coronal configuration plays an important role. If this quantity would be reversed in the simulation, and if the evolution would be seen from the same viewing angle as in Figures 3 and 4, we expect the second reconnected (pink) loop system to form on the left-hand side of the first (red) one, and the blue reconnected field lines above the nullpoint to develop an elbow which bends away from the prominence flux rope rather than toward it. It would therefore be interesting to study how the system behaves if intermediate orientations of the emerging rope are chosen.

Our results underline the importance of a precise examination of the magnetic topology (and of its formation) for the understanding of many dynamic events in the solar corona. Without a detailed consideration of the topology, it would have been very difficult to understand the complex sequence of dynamic features occurring in the simulation and in the observed event.

We thank the referee for detailed comments and suggestions which helped very much to improve the quality of this paper. Financial support by the European Commission through the SOLAIRE Network (MTRN-CT-2006-035484) and through the FP7 SOTERIA project (Grant Agreement no. 218816) are gratefully acknowledged. *Hinode* is a Japanese mission developed and launched by ISAS/JAXA, with NAOJ as domestic partner and NASA and STFC (UK) as international partners. It is operated by these agencies in co-operation with ESA and the NSC (Norway). L.G. and K.K.R. are supported by NASA under contract NNM07AB07C to SAO. We thank all the people who collaborate actively within the JOP 178 observations campaign, particularly T. Berger and the *Hinode* team, G. Molodij and the Meudon Solar Tower observers, P. Mein for reducing the MSDP data, and T. Roudier and N. Labrosse for the coordination and the pointing of the observations. T.T. thanks Y. Fan for several discussions on "kinematic flux emergence." We also thank P. Démoulin, B. Kliem, and E. Pariat for very helpful comments on this work. Our MHD calculations were done on the dual-core quadri-Opteron computers of the Service Informatique de l'Observatoire de Paris (SIO).

REFERENCES

Antiochos, S. K. 1998, ApJ, 502, L181
Archontis, V., Galsgaard, K., Moreno-Insertis, F., & Hood, A. W. 2006, ApJ, 645, L161
Asai, A., Shibata, K., Hara, H., & Nitta, N. V. 2008, ApJ, 673, 1188
Aulanier, G., DeLuca, E. E., Antiochos, S. K., McMullen, R. A., & Golub, L. 2000, ApJ, 540, 1126
Aulanier, G., & Démoulin, P. 1998, A&A, 329, 1125
Aulanier, G., Démoulin, P., & Grappin, R. 2005, A&A, 430, 1067
Aulanier, G., Pariat, E., Démoulin, P., & Devore, C. R. 2006, Sol. Phys., 238, 347
Aulanier, G., et al. 2007, Science, 318, 1588
Bateman, G. 1978, MHD Instabilities (Cambridge, MA: MIT Press)
Cirtain, J. W., et al. 2007, Science, 318, 1580
Craig, I. J. D., & McClymont, A. N. 1991, ApJ, 371, L41
Démoulin, P., Hénoux, J. C., Priest, E. R., & Mandrini, C. H. 1996, A&A, 308, 643
Démoulin, P., van Driel-Gesztelyi, L., Schmieder, B., Hemoux, J. C., Csepura, G., & Hagyard, M. J. 1993, A&A, 271, 292
Dudík, J., Aulanier, G., Schmieder, B., Bommier, V., & Roudier, T. 2008, Sol. Phys., 248, 29
Fan, Y., & Gibson, S. E. 2003, ApJ, 589, L105
Fan, Y., & Gibson, S. E. 2007, ApJ, 668, 1232
Feynman, J., & Martin, S. F. 1995, J. Geophys. Res., 100, 3355
Filippov, B. 1999, Sol. Phys., 185, 297
Filippov, B., Golub, L., & Koutchmy, S. 2009, Sol. Phys., 254, 259
Fletcher, L., Metcalf, T. R., Alexander, D., Brown, D. S., & Ryder, L. A. 2001, ApJ, 554, 451
Gibson, S. E., & Fan, Y. 2006, J. Geophys. Res. (Space Phys.), 111, 12103
Golub, L., et al. 2007, Sol. Phys., 243, 63
Gombosi, T. I., Powell, K. G., & de Zeeuw, D. L. 1994, J. Geophys. Res., 99, 21525
Heinzel, P., et al. 2008, ApJ, 686, 1383
Heyvaerts, J., Priest, E. R., & Rust, D. M. 1977, ApJ, 216, 123
Isenberg, P. A., & Forbes, T. G. 2007, ApJ, 670, 1453
Karpen, J. T., Antiochos, S. K., Devore, C. R., & Golub, L. 1998, ApJ, 495, 491
Keppens, R., Nool, M., Tóth, G., & Goedbloed, J. P. 2003, Comput. Phys. Commun., 153, 317
Kliem, B., Karlický, M., & Benz, A. O. 2000, A&A, 360, 715
Kliem, B., & Török, T. 2006, Phys. Rev. Lett., 96, 255002
Kosugi, T., et al. 2007, Sol. Phys., 243, 3
Lau, Y.-T., & Finn, J. M. 1990, ApJ, 350, 672
Low, B. C., & Hundhausen, J. R. 1995, ApJ, 443, 818
Masson, S., Pariat, E., Aulanier, G., & Schrijver, C. J. 2009, ApJ, 700, 559
Moreno Insertis, F., Galsgaard, K., & Ugarte-Urra, I. 2008, ApJ, 673, L211
Murray, M. J., van Driel-Gesztelyi, L., & Baker, D. 2009, A&A, 494, 329
Nishizuka, N., Shimizu, M., Nakamura, T., Otsuji, K., Okamoto, T. J., Katsukawa, Y., & Shibata, K. 2008, ApJ, 683, L83
Nistico, G., Bothmer, V., Patsourakos, S., & Zimbardo, G. 2009, arXiv:0906.4407
Pariat, E., Antiochos, S. K., & DeVore, C. R. 2009, ApJ, 691, 61
Patsourakos, S., Pariat, E., Vourlidas, A., Antiochos, S. K., & Wuelser, J. P. 2008, ApJ, 680, L73
Pontin, D. I., Bhattacharjee, A., & Galsgaard, K. 2007, Phys. Plasmas, 14, 052106
Priest, E. R., & Forbes, T. G. 2002, A&A Rev., 10, 313
Sato, T., & Hayashi, T. 1979, Phys. Fluids, 22, 1189
Schmieder, B., Shibata, K., van Driel-Gesztelyi, L., & Freeland, S. 1995, Sol. Phys., 156, 245
Schrijver, C. J., Elmore, C., Kliem, B., Török, T., & Title, A. M. 2008, ApJ, 674, 586
Shibata, K., Nitta, N., Strong, K. T., Matsumoto, R., Yokoyama, T., Hirayama, T., Hudson, H., & Ogawara, Y. 1994, ApJ, 431, L51
Shibata, K., Nozawa, S., & Matsumoto, R. 1992a, PASJ, 44, 265
Shibata, K., Shimojo, M., Yokoyama, T., & Ohyama, M. 1997, in ASP Conf. Ser. 111, Magnetic Reconnection in the Solar Atmosphere, ed. R. D. Bentley & J. T. Mariska (San Francisco, CA: ASP), 29
Shibata, K., et al. 1992b, PASJ, 44, L173
Titov, V. S., & Démoulin, P. 1999, A&A, 351, 707
Török, T., & Kliem, B. 2003, A&A, 406, 1043
Török, T., & Kliem, B. 2005, ApJ, 630, L97
Török, T., & Kliem, B. 2007, Astron. Nachr., 328, 743
Török, T., Kliem, B., & Titov, V. S. 2004, A&A, 413, L27
Ugarte-Urra, I., Warren, H. P., & Winebarger, A. R. 2007, ApJ, 662, 1293
van Ballegooijen, A. A. 2004, ApJ, 612, 519
Yokoyama, T., & Shibata, K. 1996, PASJ, 48, 353
Yokoyama, T., & Shibata, K. 1999, in AIP Conf. Ser. 471, ed. S. T. Suess, G. A. Gary, & S. F. Nerney (Melville, NY: AIP), 61